Electronic Supplementary Information

Experimental Section

Materials: Metal-tetramethoxyphenylporphyrin (MTMPP) and TMPP were obtained from Sigma-Aldrich. Carbon nanotube (CNT) were obtained from Suzhou-tanfeng-CNT-006-3. N,N-Dimethylformamide（DMF） was obtained from Aladdin. Isopropyl alcohol (IPA) and carbon paper were bought from Beijing Chemical Corporation. Nafion (5 wt%) were purchased from Sigma-Aldrich Chemical Reagent Co., Ltd. The water used throughout all experiments was purified through a Millipore system.

Sample preparation: To prepare MTMPP MDEs, 30 mg CNT were dispersed in 20 ml DMF by sonication for 1 h (Kunshan KQ2200DE, 100 W). A calculated amount of the original or substituted MTMPP was dissolved in 10 ml DMF with high-power sonication and added to the CNT suspension. The mixed suspension was sonicated for another 30 min and stirred at room temperature for 24 h. MTMPP has low solubility in DMF, and thus the high-power sonication step is important for mixing. The MTMPP MDE materials were separated by centrifuge and washed with DMF, ethanol and water (Milli-Q water with a resistivity of 18.2 MΩ cm at 25 °C was used throughout the experiments), followed by lyophilization to obtain the final products.

Characterizations: FTIR spectrum was taken on a BRUKER-EQUINOX-55 IR spectrophotometer. High-resolution transmission electron microscopy (HRTEM) images were obtained from a Zeiss Libra 200FE transmission electron microscope operated at 200 kV. Elemental analysis was performed using ICP–MS (Teledyne Leeman Labs). XPS measurements were performed on an ESCALABMK II X-ray photoelectron spectrometer using Mg as the exciting source. The absorbance data of spectrophotometer were acquired on SHIMADZU UV-1800 UV-Vis spectrophotometer. In situ ATR-FTIR measurements were taken on a BRUKER-EQUINOX-55 IR spectrophotometer, a diamond-like carbon was coated onto a Si wafer ($5 \times 8 \times 1 mm^3$) to prepare the internal reflection element (IRE). The coated IRE

was ultrasonicated for 2 min with 30% concentrated H_2SO_4 followed by rinsing with DI water before experiments. A 50 μL of 2mg mL^{-1} catalyst ink (no Nafion binder) was dropcast on the IRE and dried under air at room temperature. A glassy carbon paper was placed on top of the catalyst layer for good electrical contact. Glassy carbon rod connected to the IRE, Pt gauze, and Ag/AgCl in 3M KCl were used as the working electrode, counter electrode, and reference electrode, respectively. An FTIR spectrometer with a mercury cadmium telluride (MCT) detector was used for the in situ ATR-FTIR measurements. 0.1 M $HClO_4$ solutions were saturated with O_2 for ORR. Gamry Reference 600 potentiostat during recording of the IR spectra.

Electrochemical test for ORR: Electrochemical measurements were performed using an electrochemical workstation (CHI760E, CH Instruments). For rotating ring disk electrode (RRDE) measurements (disk area: 0.2475 cm^2 ； ring area：0.1866 cm^2), a three-electrode system was built with an RRDE (glassy carbon (GC) disk + Pt ring), a Ag/AgCl (saturated KCl solution) reference electrode, and a Pt foil counter electrode. The RRDE was polished with 1um alumina aqueous suspension for 5 min and 0.05um alumina aqueous suspension for 5 min and ultra-sonicated in DI water for 30 s. Pt ring was then electrochemically cleaned in the same potential range. The H_2O_2 production activity was assessed by linear sweep voltammetry (LSV) in O_2-saturated 0.1 M $HClO_4$ and 0.1 M PBS at a scan rate of 20 mV s^{-1} and a rotation speed of 1600 rpm. During the LSV, the Pt ring potential was held at 1.2 V (vs. RHE). The H_2O_2 selectivity was calculated using the following relation:

$$H_2O_2\ (\%) = 200 \times I_r / N / (I_d + I_r / N)$$

where I_r is the ring current, I_d is the disk current and N is the collection efficiency (0.325).

The electrogeneration of H_2O_2: The electrogeneration of H_2O_2 were conducted in two electrode system in a cell with nafion 117 membrane as separator. The cathode compartment (30ml) and anode compartment (30 mL) are filled with 0.1 M $HClO_4$ or 0.1 M PBS at 25 ^oC. Cathode were prepared by depositing catalyst ink (0.05 mg cm^{-2}) on a carbon paper (1 by 1 cm).

To quantify the H_2O_2 produced, the samples was collected at certain time and

mixed with same volume of titanium oxysulfate solution (6 g L^{-1}). The H_2O_2 yield was measured by using the indicator of titanium oxysulfate. The generated complex compound solution was detected with UV−vis spectrophotometer (UV-8000, METASH.) at the maximum absorption wavelength λ = 406 nm.

The cell FE for H_2O_2 production is calculated as follow:

$$FE_{cell} = \frac{\text{generated } H_2O_2 \text{ (mol)} \times 2 \times 96485}{\text{total amount of charge passed (C)}} \times 100 \text{ (maximum 200\%)}$$

Calculation details: We have performed spin-polarized density functional theory (DFT) calculations via Vienna ab initio simulation package (VASP).[1] Projected augment wave (PAW) pseudopotential[2] was used to account for the interaction between valence electrons and ion cores, and Perdew, Burke, and Ernzerhof (PBE) functional[3] for the exchange-correlation effect. The van der Waals (vdW) interaction was included by using the DFT-D3 method.[4] The kinetic energy cutoff of 450 eV was adopted for the plane-wave basis. The convergence criteria for the total energy and the Hellmann-Feynman force are 10^{-4} eV and 0.02 eVÅ^{-1}, respectively. To account for the on-site coulomb interaction for the localized 3*d* electrons, DFT + U through the rotationally invariant approach[5] was adopted, for which the effective U values for different transition metals are taken from Ref.[6] and listed in Supplementary Table S4. For the bare and adsorbed transition-metal TMPP molecules, the box with the size of 36×36×20 Å^3 has been used with the vacuum space between the molecule and its images larger than 15 Å along all directions to decouple their interaction, for which the 1×1×1 Monkhorst-Pack grid was used to sample the first Brillouin zone.[7]

The computational hydrogen electrode (CHE) model was adopted to study the $2e^-$ and $4e^-$ ORR processes on the various transition-metal TMPP molecules,[8] using the equation: $\Delta G = \Delta E + \Delta E_{ZPE} - T\Delta S + \Delta G_U$. In the equation, E, E_{ZPE}, and S denote the total electronic energy, zero-point energy, and entropy, respectively, and the temperature (T) is taken as 298.15 K. E_{ZPE} and S (listed in Table S5) of the adsorbed intermediates were obtained from DFT calculations, while those of the free molecules taken from the NIST databases.[9] ΔG_U is equal to $-neU$, where U is the applied electrode potential, e is the elementary charge transferred, and n is the number of

proton–electron pairs transferred. The solvation corrections were applied in accordance with previous studies,[6,10,11] where OH* and OOH* are stabilized by 0.30 eV (the asterisk (*) denotes the adsorption site). The $2e^-$ and $4e^-$ ORR to produce H_2O_2 and H_2O, respectively, were considered to follow the associative mechanisms. The $2e^-$ ORR consists of two elementary steps (a and b):

$$* + O_2\,(g) + H^+ + e^- \rightarrow OOH* \qquad (a)$$

$$OOH* + H^+ + e^- \rightarrow H_2O_2\,(l) + * \qquad (b)$$

The $4e^-$ ORR consists of four elementary steps (c, d, e, and f):

$$* + O_2\,(g) + H^+ + e^- \rightarrow OOH* \qquad (c)$$

$$OOH* + H^+ + e^- \rightarrow O* + H_2O\,(l) \qquad (d)$$

$$O* + H^+ + e^- \rightarrow OH* \qquad (e)$$

$$OH* + H^+ + e^- \rightarrow H_2O\,(l) + * \qquad (f)$$

The descriptor φ is adapted from Ref.[6] correlating with the binding free energy of the relevant intermediates (OOH*, O*, and OH*), which only contains the intrinsic properties of the active center and is defined as:

$$\varphi = \theta_d \times \frac{E_M + \alpha \times n_N \times E_N}{E_O} \qquad (g)$$

In (g), E_M and θ_d denotes the electronegativity of the metal element and its valence electron number in the *d* orbital derived from the periodic table. n_N is the number of the coordinated N atoms of the metal center. E_N and E_O represent the element electronegativity of N and O, respectively. α is the correction coefficient and set to 1.25.[6]

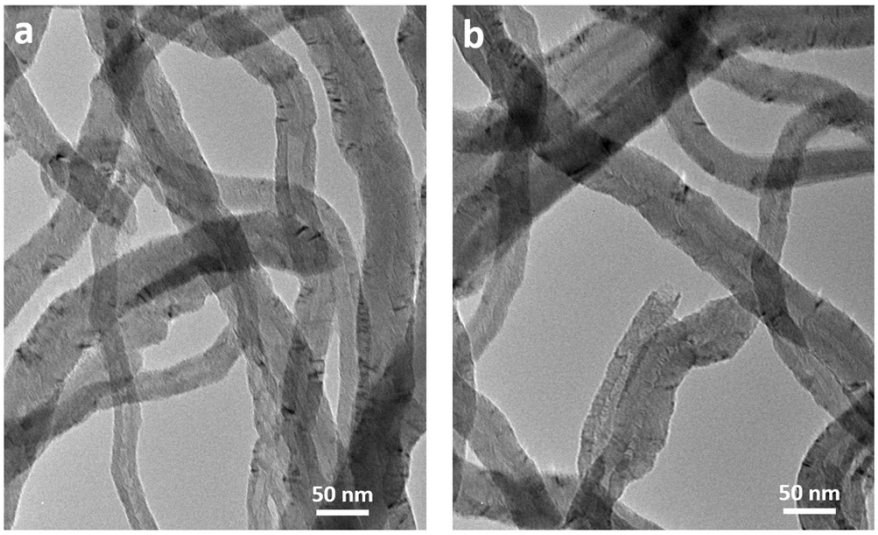

Fig. S1. Typical TEM images of (a) CNT and (b) CoTMPP/CNT.

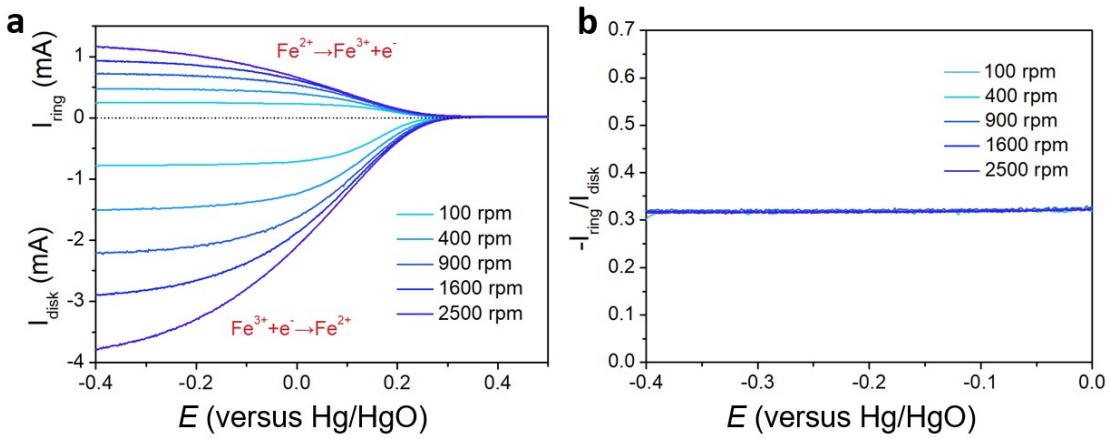

Fig. S2. Calibration of the collection efficiency of the RRDE by the redox of potassium ferricyanide.

Note: An electrolyte containing 10 mM potassium ferricyanide ($K_3Fe(CN)_6$) and 1 M KCl was prepared by dissolving 1 mM $K_3Fe(CN)_6$ and 0.1 M KCl in 100 mL ultra-pure water and deoxygenated by bubbling N_2. The redox of $K_3Fe(CN)_6$ was evaluated in a three-electrode configuration with Pt plate as the counter electrode and Hg/HgO electrode with saturated KCl salt bridge as the reference electrode on a rotating ring disk electrode (RRDE) setup. The potential of the disk was scanned from 0.5 V to 0 V vs. Hg/HgO electrode to reduce Fe^{3+} to Fe^{2+} while the potential of the Pt ring was maintained at 0.5 V vs. Hg/HgO electrode to oxidize Fe^{2+} to Fe^{3+}. The collection efficiency (CE) of the RRDE was calculated as $CE = -I_{Ring}/I_{Disk}$, where I_{Ring} is the current on Pt ring and I_{Disk} is the current on glassy carbon disk.

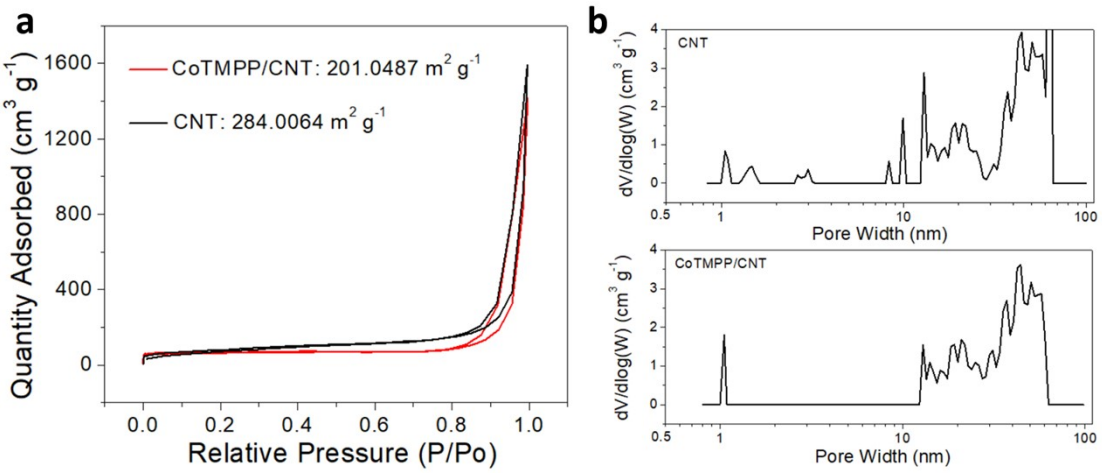

Fig. S3. (a) Nitrogen adsorption−desorption isotherms and (b) relevant pore-size distribution of CoTMPP/CNT and CNT. The specific surface area of CoTMPP/CNT is slightly smaller than that of CNT, mesopores disappear and micropores increase, possibly due to the micropore defects generated during reaction process.

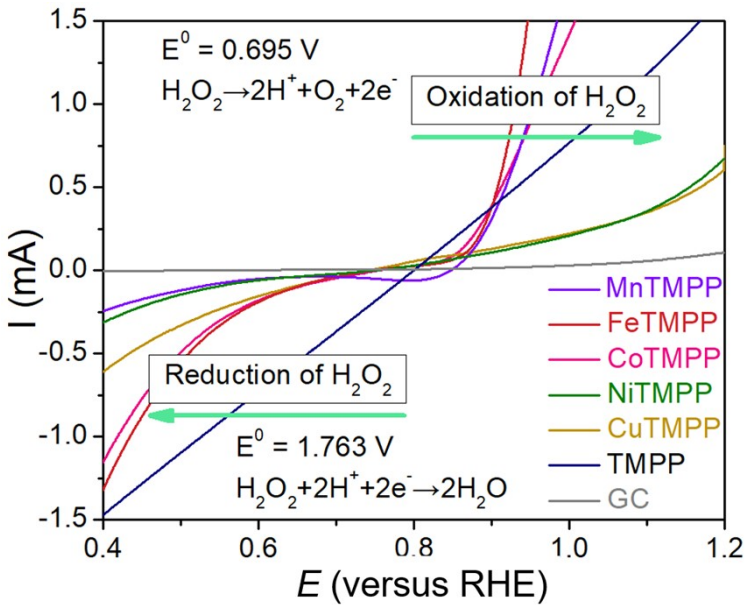

Fig. S4. LSV curves of the MTMPP/CNT and blank glassy carbon electrode (GC) in N_2 saturated electrolyte containing 0.1 M $HClO_4$ and 0.1 M H_2O_2.

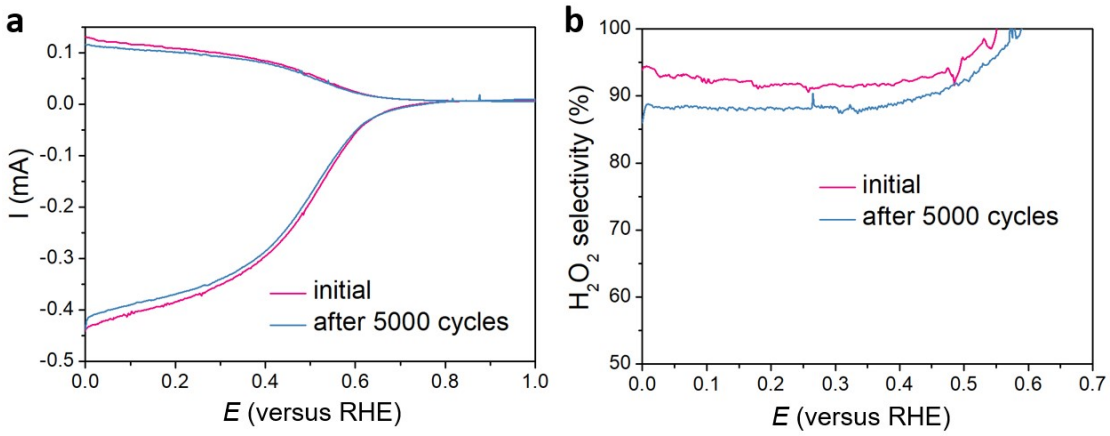

Fig. S5. (a) LSV curves of CoTMPP/CNT after 5000 cycles at 1600 rpm in O_2-saturated 0.1 M $HClO_4$, and (b) corresponding H_2O_2 selectivity.

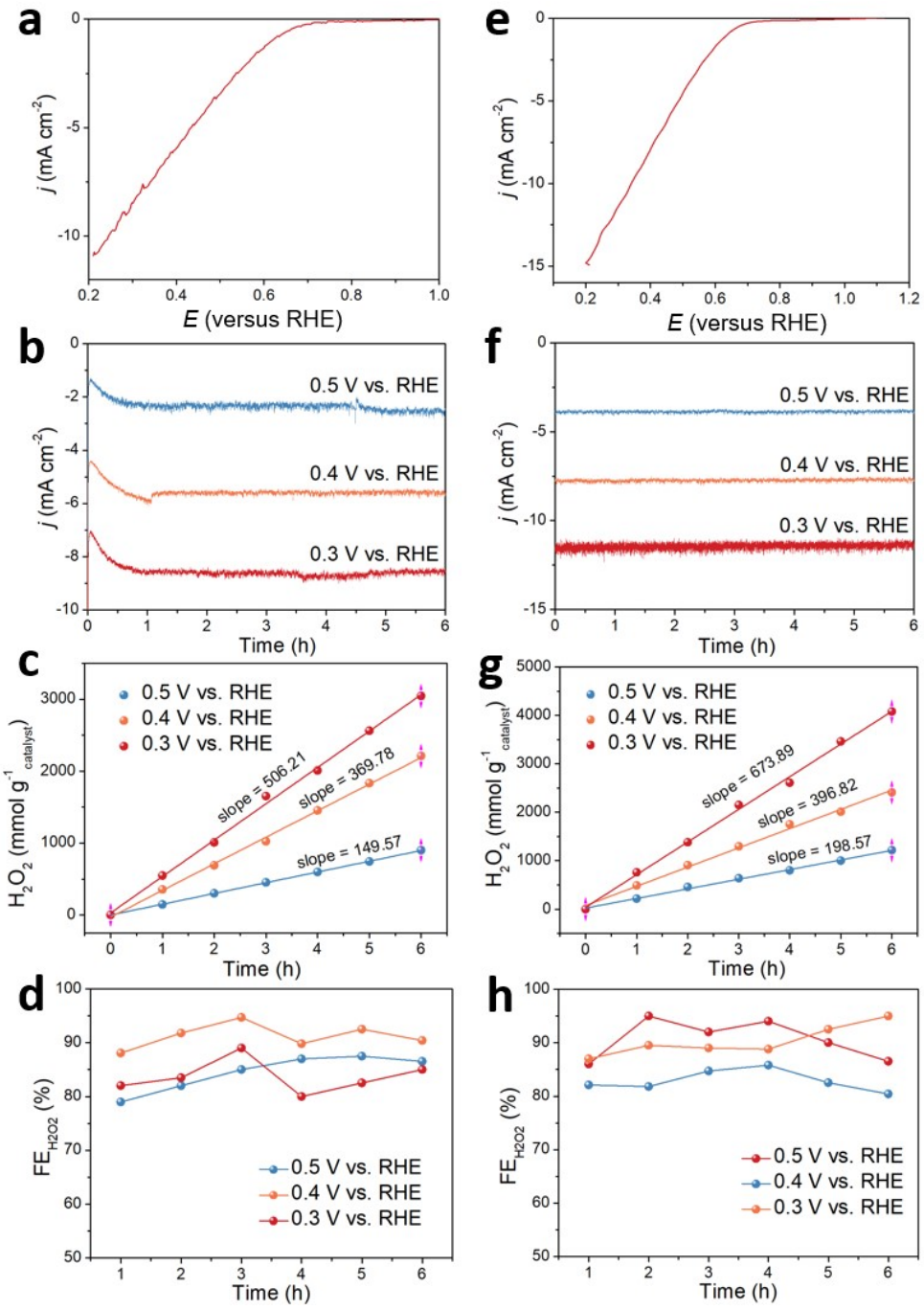

Fig. S6. Half-cell experiment for fixed potential chronoamperometry of CoTMPP/CNT (a-d in 0.1 M $HClO_4$, e-h in 0.1 M PBS): (a,e) Polarization curve (without IR-compensation), (b,f) current density along with time at different potential, (c,g) average formation rate of H_2O_2, (d,h) Faraday efficiency (FE) of H_2O_2 along with time.

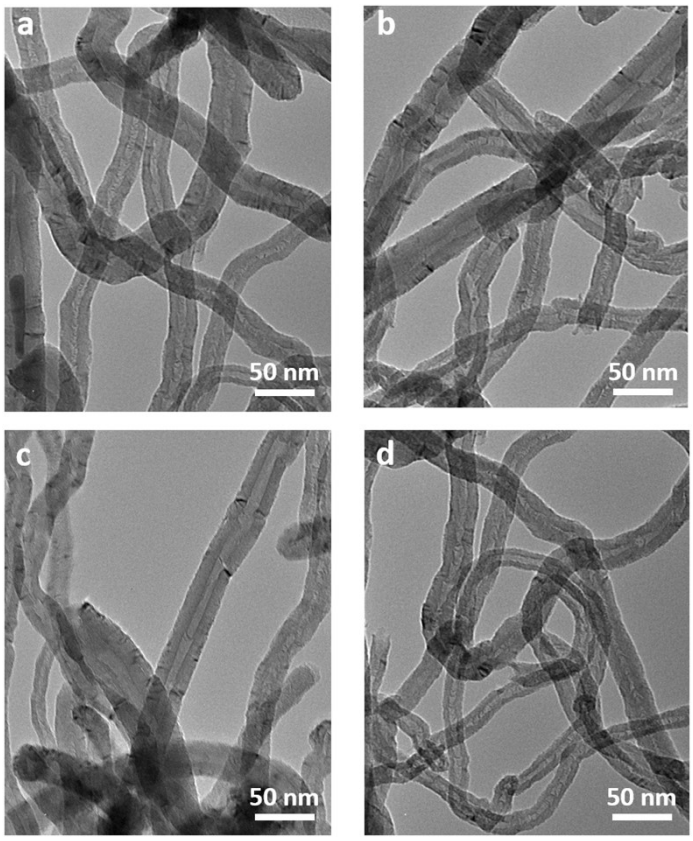

Fig. S7. Typical TEM images of (a) MnTMPP/CNT, (b) FeTMPP/CNT, (c) NiTMPP/CNT, and (d) CuTMPP/CNT.

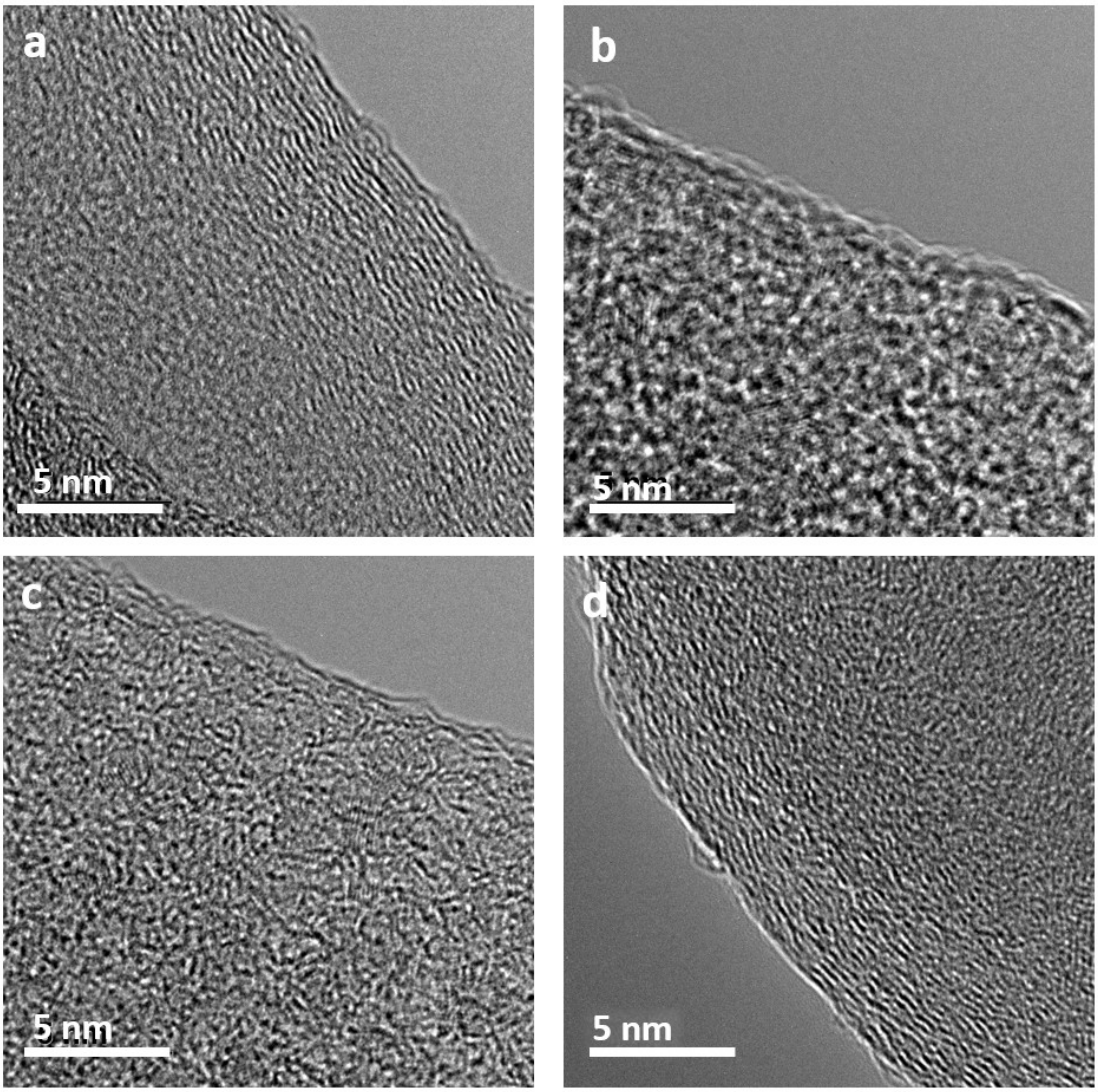

Fig. S8. HRTEM images of (a) MnTMPP/CNT, (b) FeTMPP/CNT, (c) NiTMPP/CNT, (d) CuTMPP/CNT.

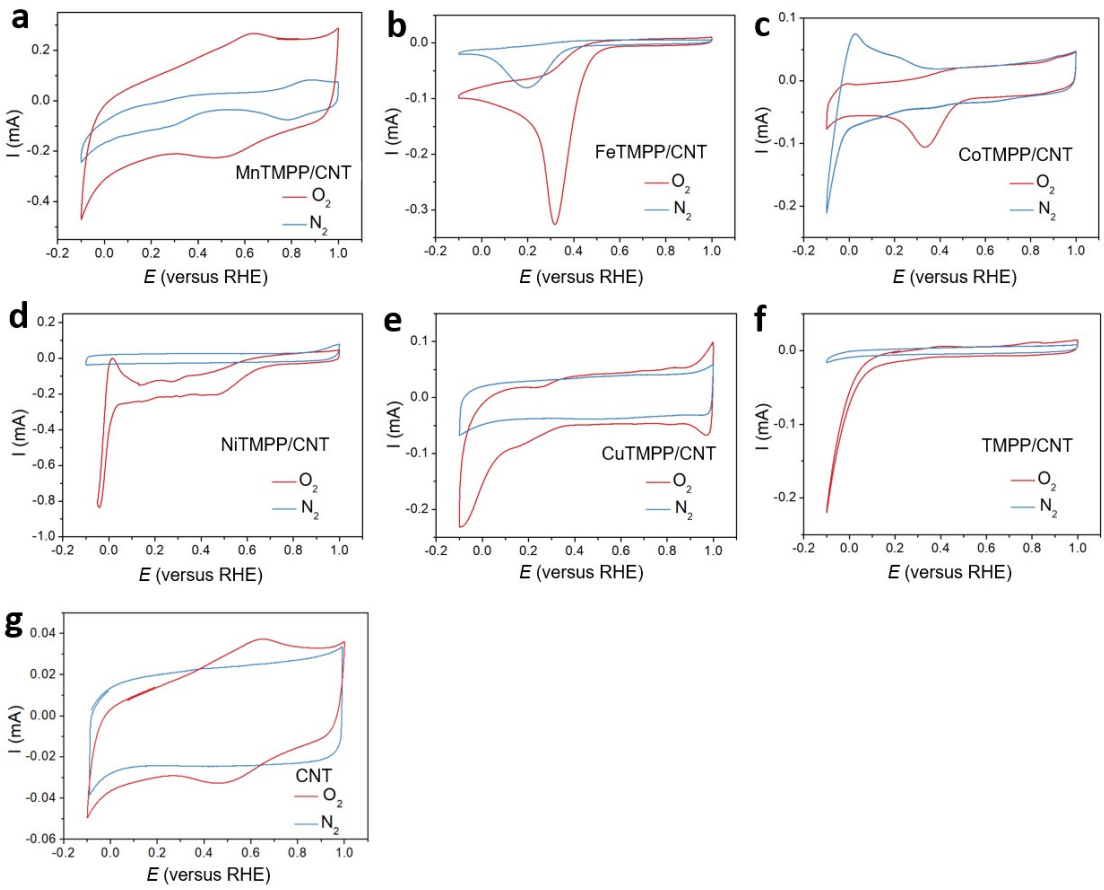

Fig. S9. CV curves for (a) MnTMPP/CNT, (b) FeTMPP/CNT, (c) CoTMPP/CNT, (d) NiTMPP/CNT, (e) CuTMPP/CNT, (f) TMPP/CNT, and (g) pristine CNT in 0.1 M $HClO_4$ solution saturated with O_2 (red lines) and N_2 (blue lines) at a scan rate of 20 mV s^{-1}.

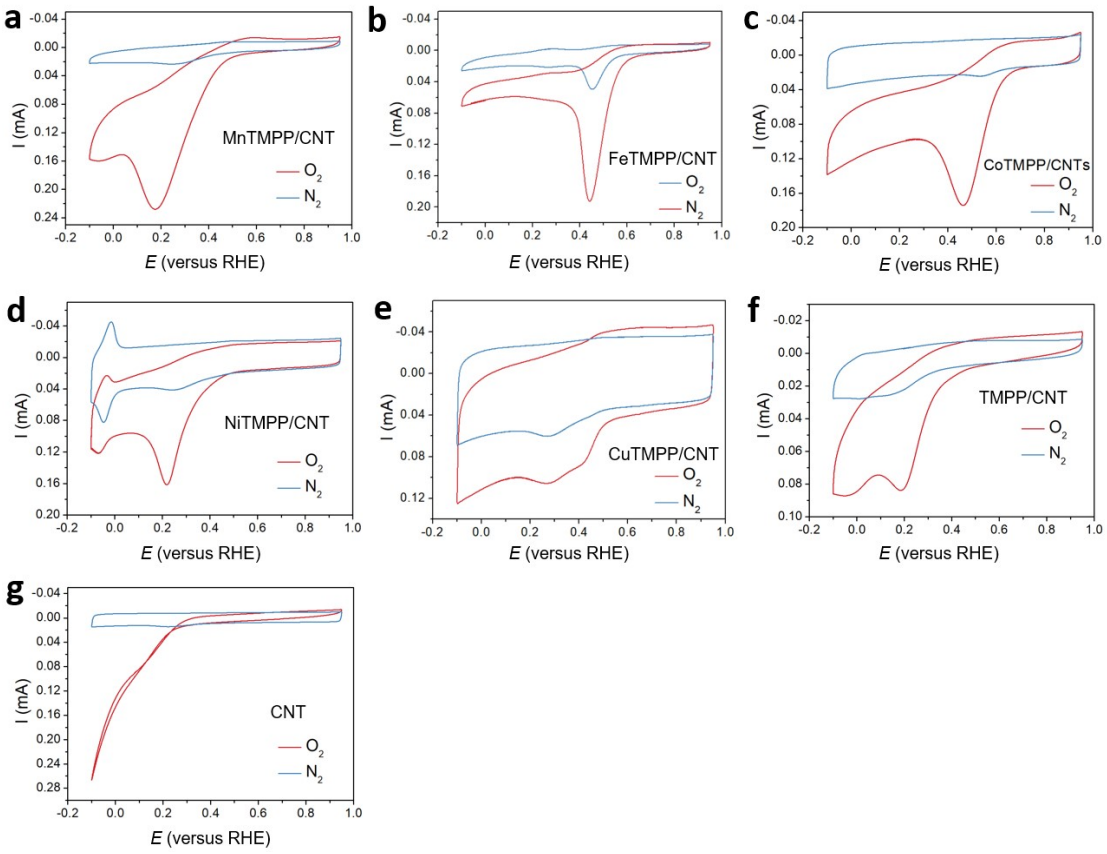

Fig. S10. CV curves acquired in O_2-saturated (red lines) and N_2-saturated (blue lines) 0.1 M PBS at a scan rate of 20 mV/s: (a) MnTMPP/CNT, (b) FeTMPP/CNT, (c) CoTMPP/CNT, (d) NiTMPP/CNT, (e) CuTMPP/CNT, (f) TMPP/CNT, and (g) CNT.

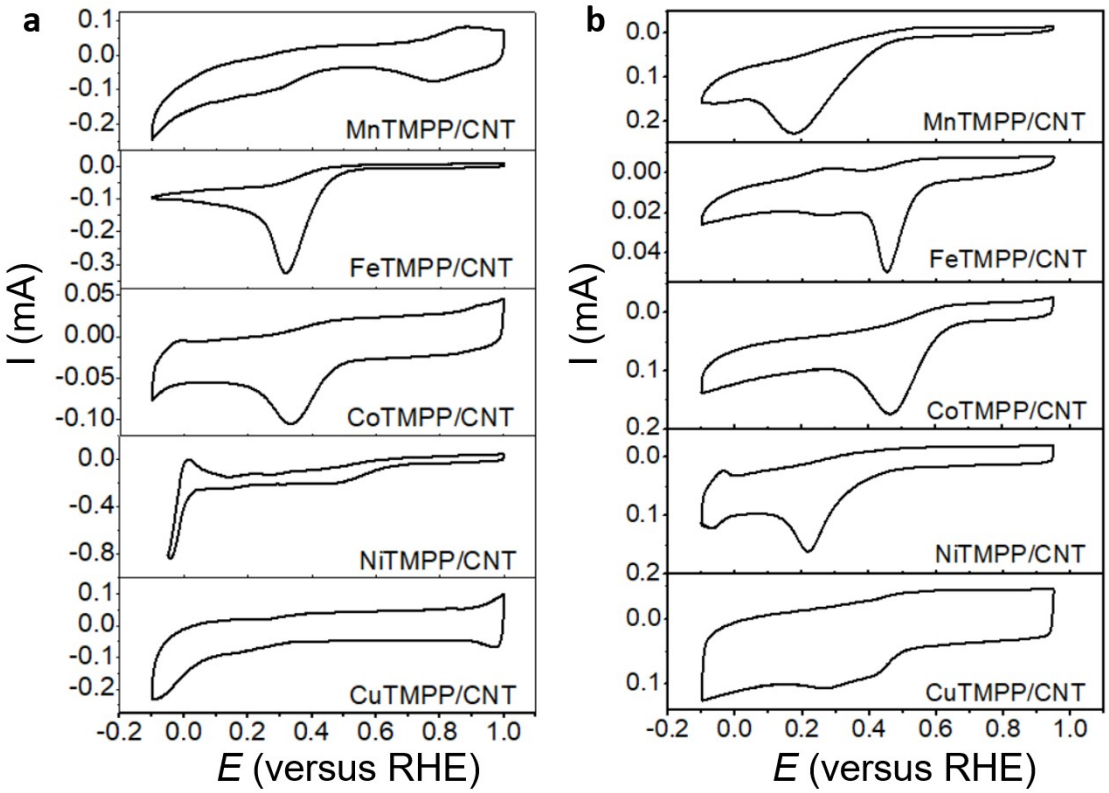

Fig. S11. CV curves acquired in O_2-saturated (a) 0.1 M $HClO_4$ and (b) 0.1 M PBS at a scan rate of 20 mV/s.

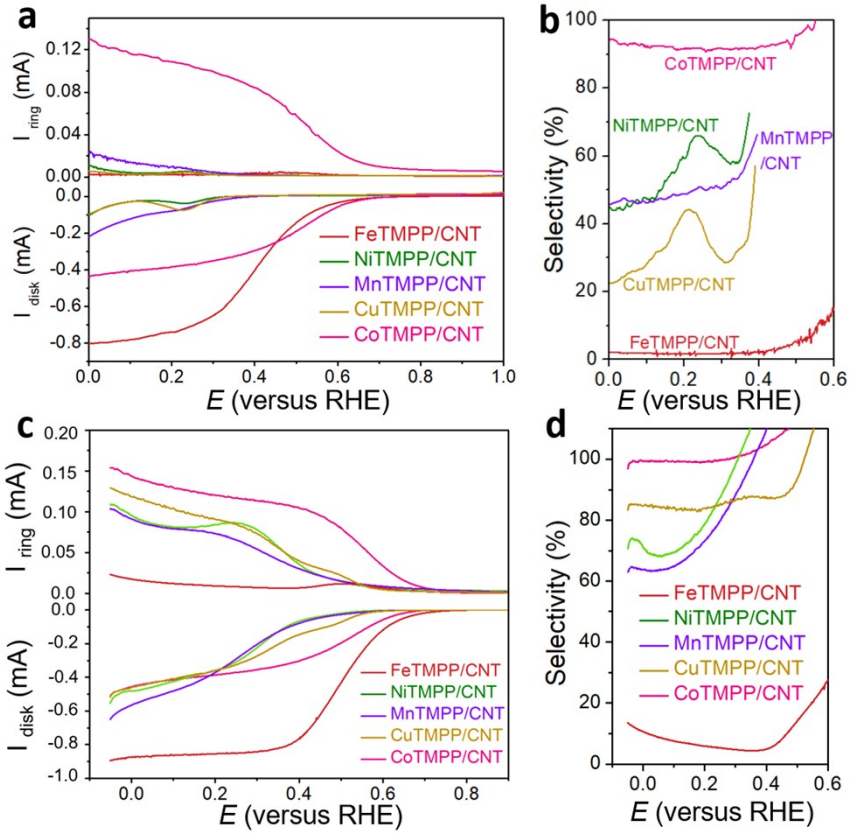

Fig. S12. LSV curves of catalysts recorded at 1600 rpm in O_2-saturated (a) 0.1 M $HClO_4$ and (c) 0.1 M PBS, and corresponding H_2O_2 selectivity in (b) 0.1 M $HClO_4$ and (d) 0.1 M PBS.

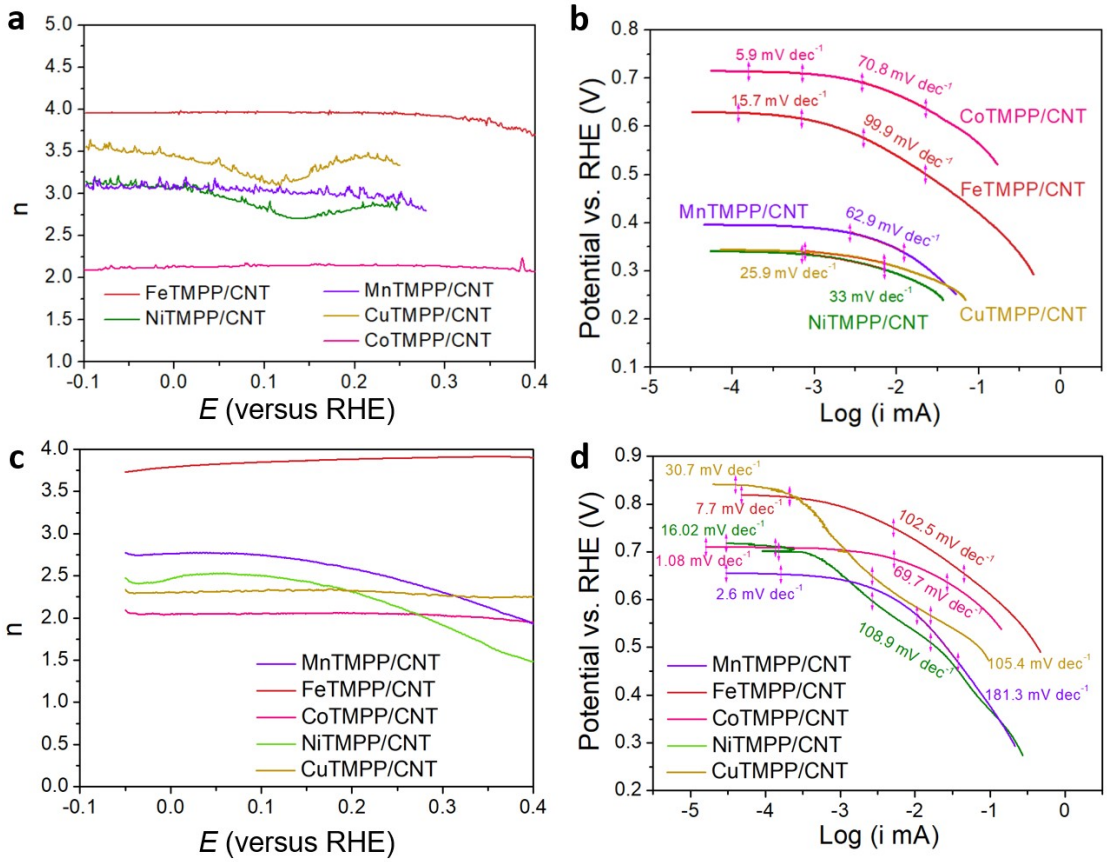

Fig. S13. The calculated electron transfer numbers of ORR over the catalysts in (a) 0.1 M $HClO_4$ and (c) 0.1 M PBS. Tafel plots of the MTMPP/CNT catalysts (Mn, Fe, Co, Ni, and Cu) in (b) 0.1 M $HClO_4$ and (d) 0.1 M PBS.

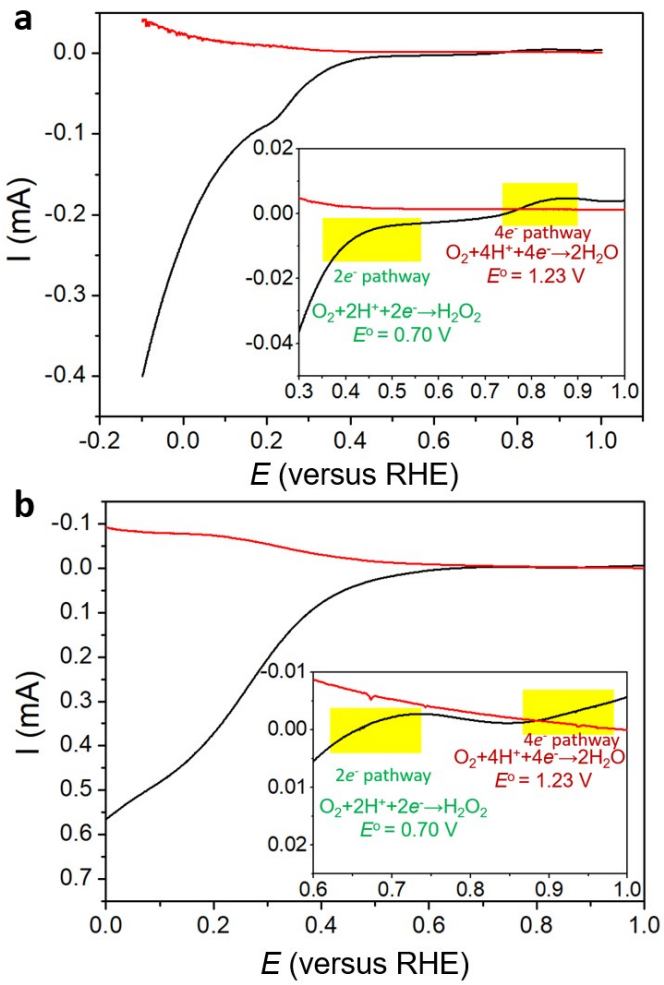

Fig. S14. LSV curves of MnTMPP/CNT recorded at 1600 rpm in O_2-saturated (a) 0.1 M $HClO_4$ and (b) 0.1 M PBS.

Note: DFT calculations indicate that MnTMPP/CNT exhibit higher catalytic activity for $4e^-$ ORR, but it was not observed in the experiment. As shown in Figure S19a, due to high oxygen affinity, MnTMPP/CNT may be covered by OH* or O* within a wide potential range versus RHE, which suggests that MnTMPP/CNT may be poisoned under the working condition and lose catalytic activity, in line with experiment.

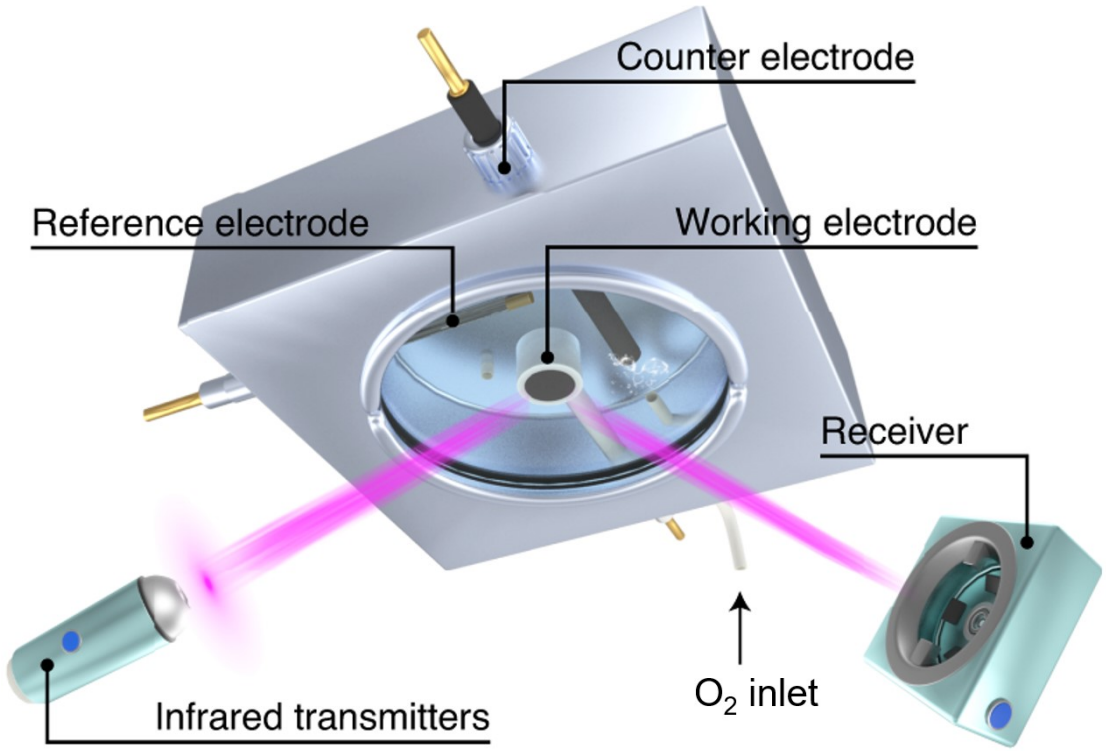

Fig. S15. Schematic of the tailor-made electrolytic cell for in situ characterization (modified from ref.[12]).

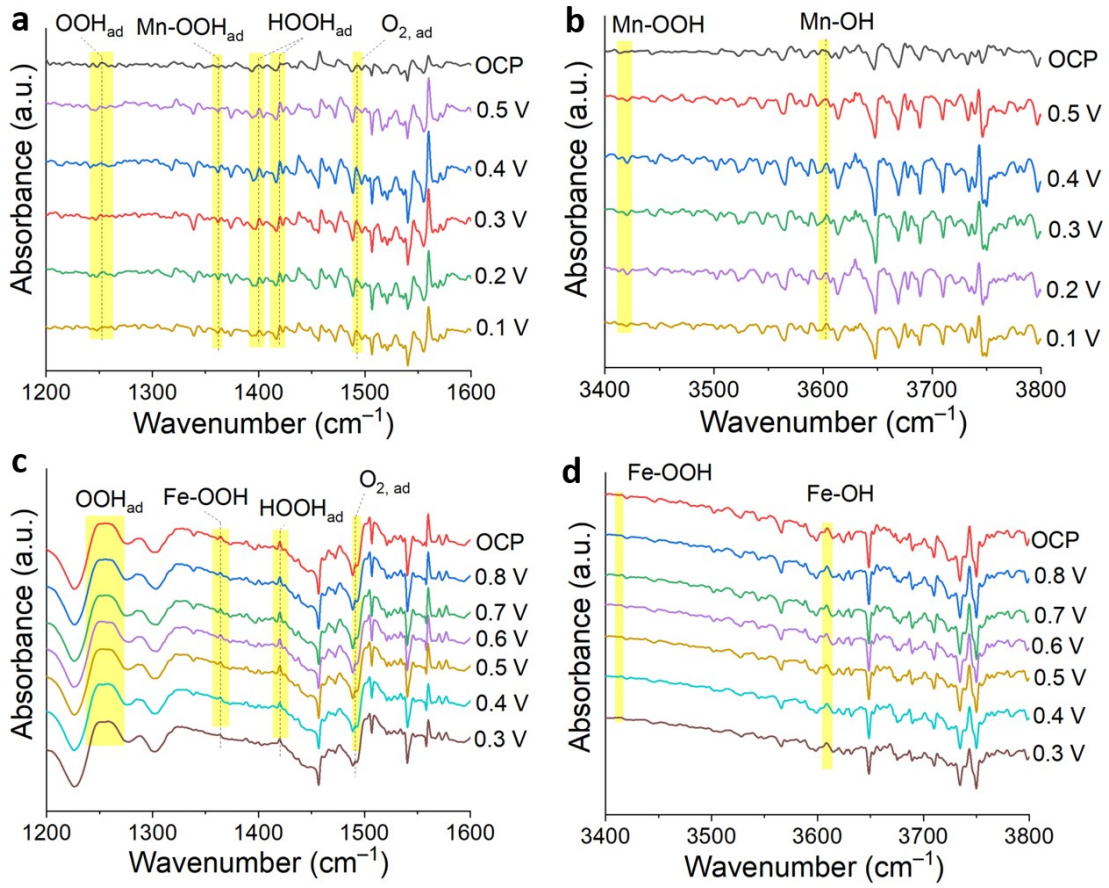
a
OOHad
Mn-OOHad
HOOHad
O2, ad
OCP
0.5 V
0.4 V
0.3 V
0.2 V
0.1 V
Absorbance (a.u.)
1200
1300
1400
1500
1600
Wavenumber (cm−1)
b
Mn-OOH
Mn-OH
OCP
0.5 V
0.4 V
0.3 V
0.2 V
0.1 V
Absorbance (a.u.)
3400
3500
3600
3700
3800
Wavenumber (cm−1)
c
OOHad
Fe-OOH
HOOHad
O2, ad
OCP
0.8 V
0.7 V
0.6 V
0.5 V
0.4 V
0.3 V
Absorbance (a.u.)
1200
1300
1400
1500
1600
Wavenumber (cm−1)
d
Fe-OOH
Fe-OH
OCP
0.8 V
0.7 V
0.6 V
0.5 V
0.4 V
0.3 V
Absorbance (a.u.)
3400
3500
3600
3700
3800
Wavenumber (cm−1)

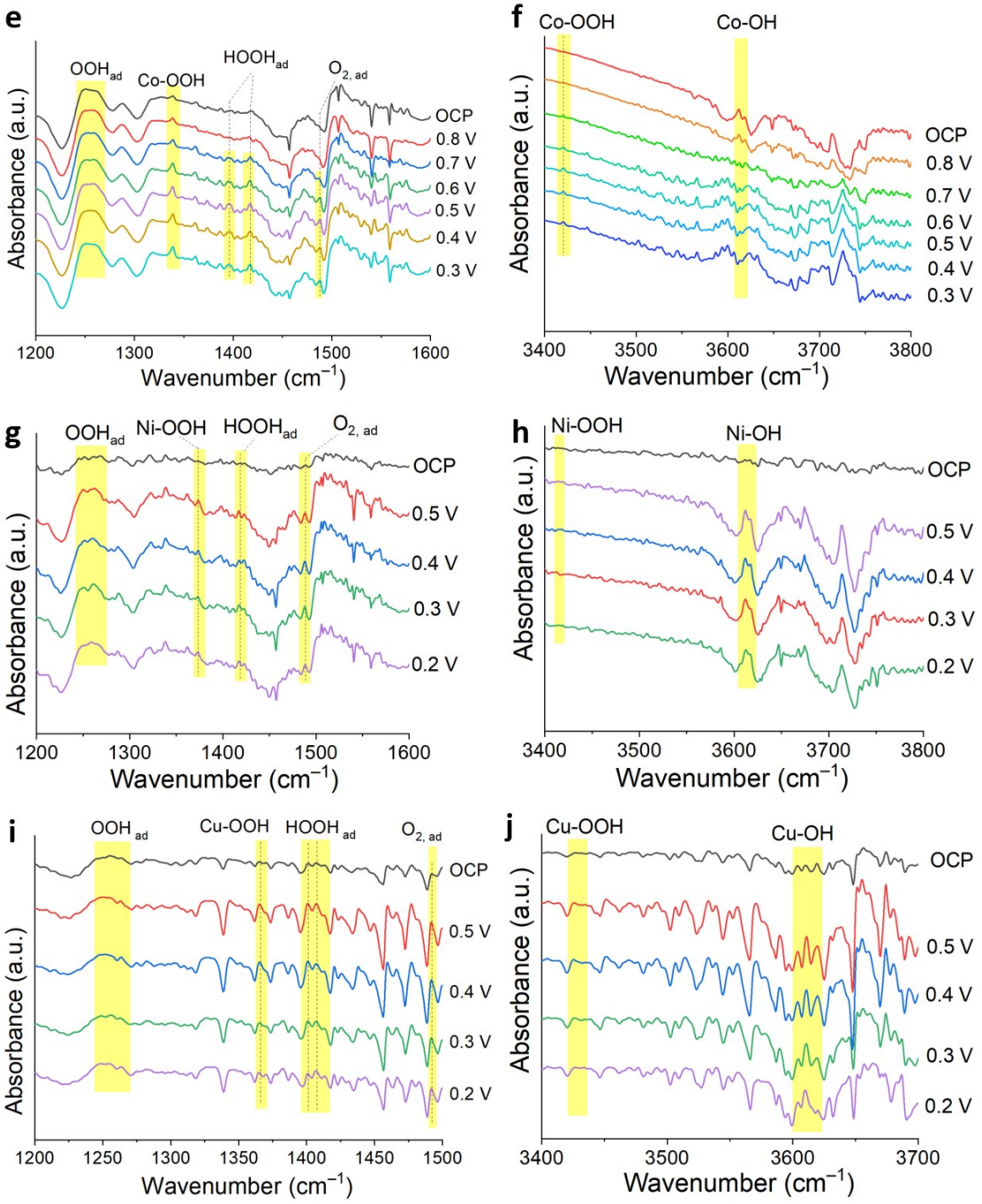

Fig. S16. In situ ATR-IR spectra at constant potential in O_2-saturated 0.1 M $HClO_4$: (a,b) MnTMPP/CNT, (c,d) FeTMPP/CNT, (e,f) CoTMPP/CNT, (g,h) NiTMPP/CNT, (i,j) CuTMPP/CNT.

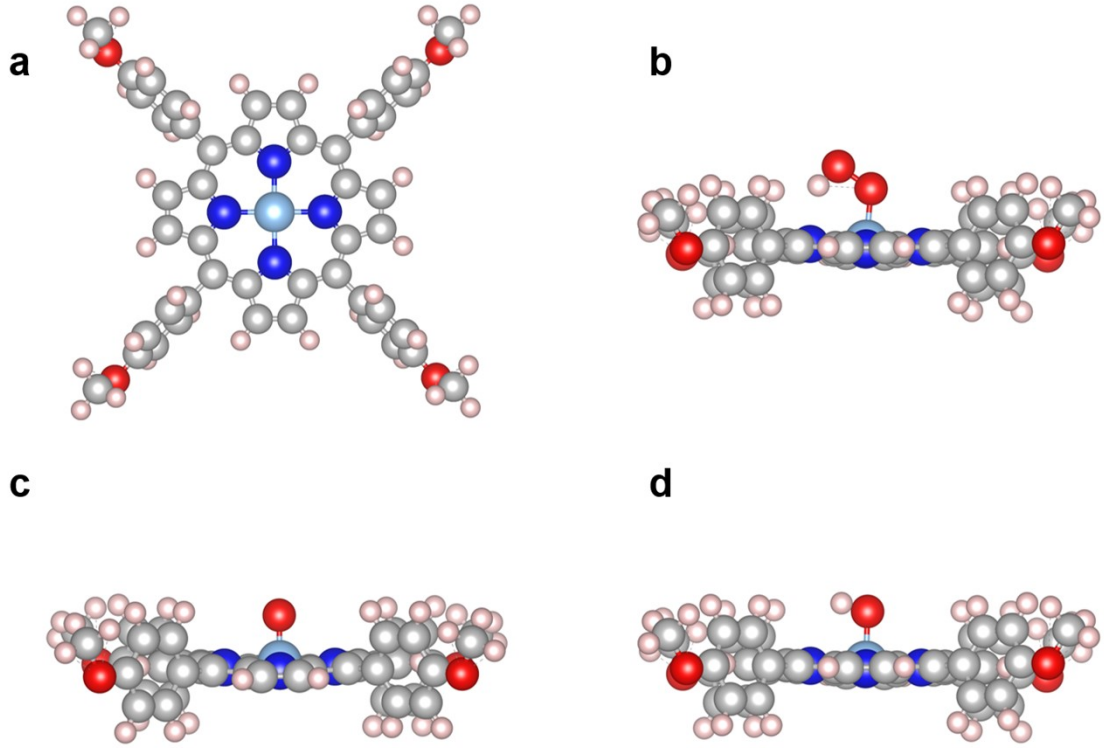

Fig. S17. (a) Optimized configuration of the considered transition-metal TMPP molecules (transition-metal = Mn, Fe, Co, Ni, and Cu). (b)-(d) The most stable configurations of OOH* (b), O* (c), and OH* (d) bonded with the metal centers of

the catalysts.

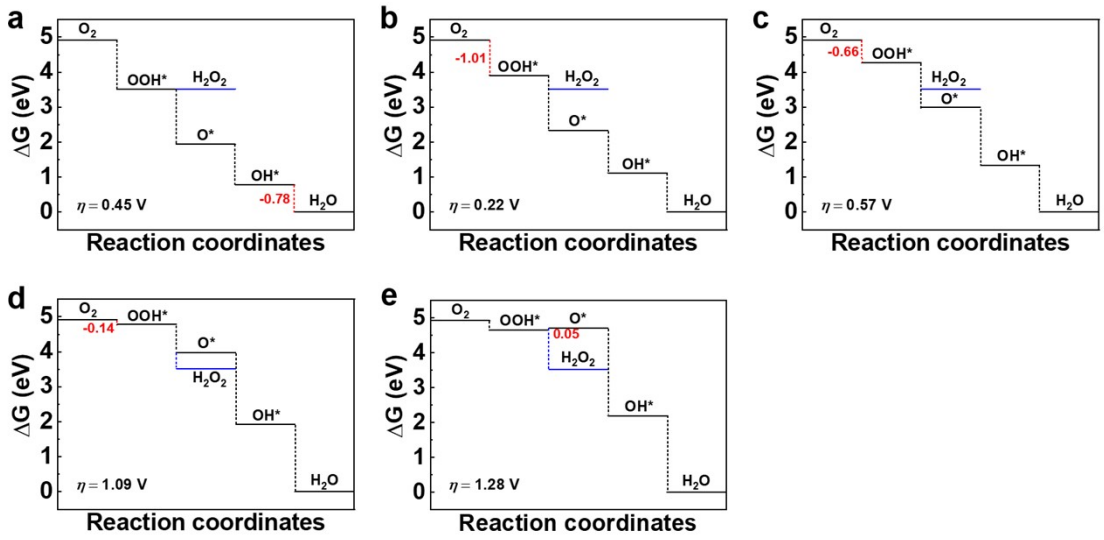

Fig. S18. Free energy diagrams at potential of 0 V versus RHE for the $2e^-$ (blue line) and $4e^-$ (black line) ORR processes on MnTMPP (a), FeTMPP (b), CoTMPP (c), NiTMPP (d), and CuTMPP (e). The theoretical overpotential (η) for the $4e^-$ ORR is given.

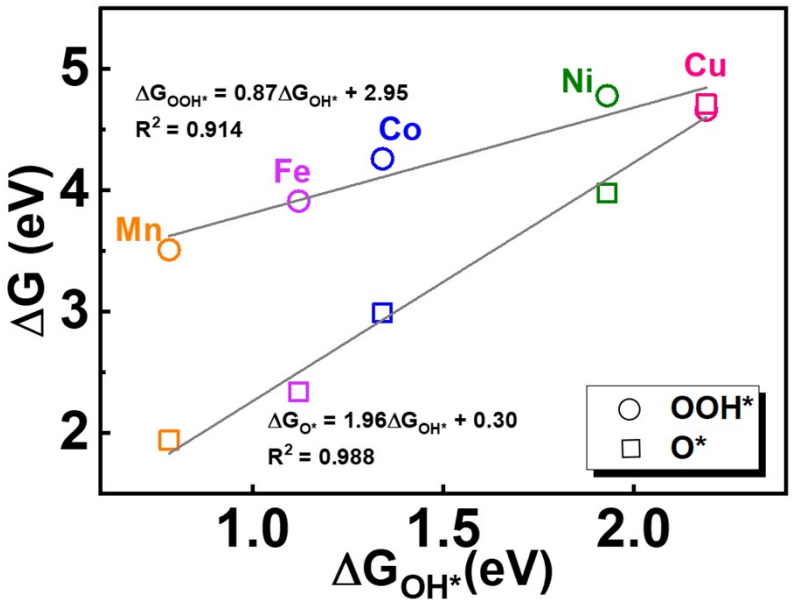

Fig. S19. Scaling relationship between the binding free energy (ΔG) of OOH* and OH*, and that between O* and OH*.

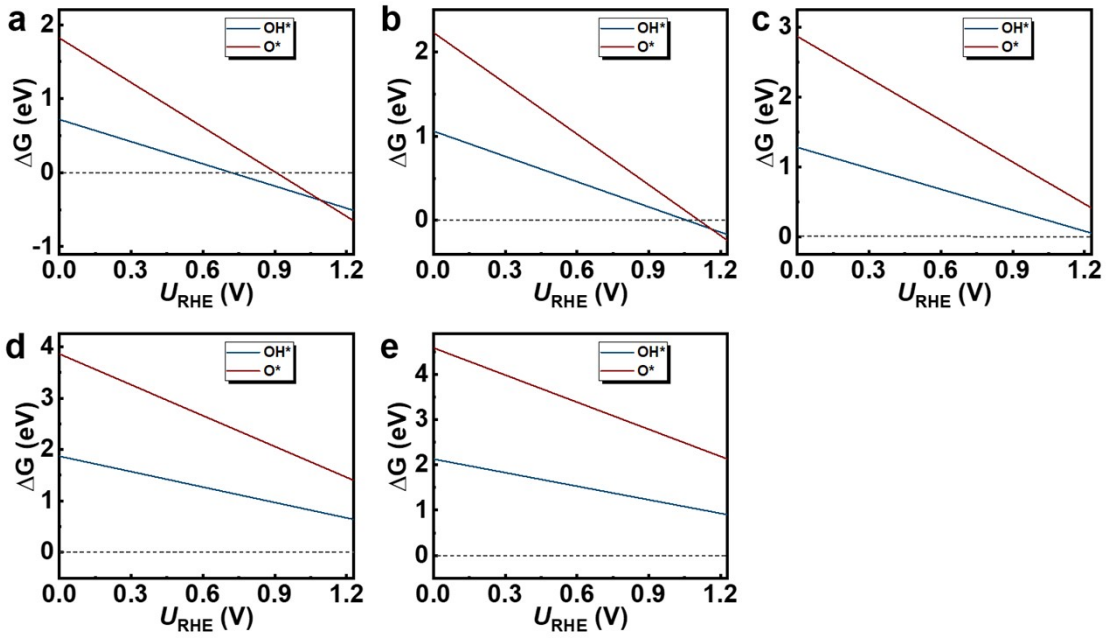

Fig. S20. Surface Pourbaix diagrams for MnTMPP (a), FeTMPP (b), CoTMPP (c), NiTMPP (d), and CuTMPP (e). Note that only the side that can interact with the reactants was considered.

Table S1. Elemental contents obtained by XPS and ICP-MS.

Sample (MTMPP /CNT)	N by XPS (at. %)	C by XPS (at. %)	O by XPS (at. %)	Metal by XPS (at. %)	Metal by XPS (wt. %)	Metal content by ICP (wt. %)
Mn	1.46	95.88	2.53	0.11	0.48	
Fe	1.79	95.74	1.93	0.23	1.01	
Co	0.70	97.66	1.65	0.08	0.37	0.32
Ni	0.63	97.23	2.10	0.09	0.41	
Cu	1.30	95.73	2.66	0.21	1.09	

Table S2. Summary of the electrocatalysts for H_2O_2 production via ORR in Figure 2e.

Catalyst	Description	Catalyst loading (ug/cm_{disk}^2)	Over potential (V)	H_2O_2 selectivity (%)	Electrolyte	Ref.
CoTMPP/CNT	cobalt-porphyrin supported carbon nanotubes	40	0 0	>95 % ~100 %	0.1 M $HClO_4$ 0.1 M PBS	This work
Co-NC	Single Co atom anchored in nitrogen doped carbon	25	0	~93	0.1 M $HClO_4$	12
Pt-Hg (pc)	Hg modified polycrystalline Pt disk	/	0.1	~91	0.1 M $HClO_4$	13
Pt-Hg/C	Carbon supported Pt-Hg nanoparticles	23	0.1	~91	0.1 M $HClO_4$	13
Pd-Hg/C	ETEK carbon supported Pd-Hg nanoparticles	17	0	~95	0.1 M $HClO_4$	14
Au-Pd/C	Vulcan XC-72 carbon supported Au-Pd nanoalloys	110	0.35	~93% @ 0.0 V	0.1 M $HClO_4$	15
Pt1/TiN	TiN supported Pt single atom catalyst	15	0.2	~60	0.1 M $HClO_4$	16
Pt1/SC	Sulfur doped zeolite-templated carbon	50	0.1	~94	0.1 M $HClO_4$	17
VC	Vulcan XC72 carbo	25000	0.4	~75	0.1 M H_2SO_4	18
g-N-CNHs	N-doped graphitized carbon nanohorns	15000	0.45	~90	0.1 M H_2SO_4	19

NMC	Nitrogen-doped mesoporous carbon	50	0.38	~95	0.5 M H_2SO_4	20
Co1–NG(O)	optimal Co–N4 moiety in nitrogen-doped graphene	100	0 0	~55 ~50	0.1 M $HClO_4$ 0.1 M PBS	21
h-Pt1-CuS_x	dispersing platinum in amorphous CuS_x support	240	0	~95	0.1 M $HClO_4$	22
PtP_2	ultrasmall and monodisperse colloidal PtP_2 nanocrystals	200	0	~98	0.1 M $HClO_4$	23
Fe-C-O	Fe single atom coordination in carbon nanotube	100	0.2	~80	0.1 M PBS	24

Tables S3. Binding free energy (ΔG) of OOH*, O*, and OH* on the metal centers of the transition-metal TMPP molecules (transition-metal = Mn, Fe, Co, Ni, and Cu).

	ΔG_{OOH*} (eV)	ΔG_{O*} (eV)	ΔG_{OH*} (eV)
Mn	3.51	1.94	0.78
Fe	3.91	2.34	1.12
Co	4.26	2.99	1.34
Ni	4.78	3.98	1.93
Cu	4.66	4.71	2.19

Table S4. The effective U values of the 3*d* orbitals for DFT + U calculations.

3d	Mn	Fe	Co	Ni	Cu
U−J	3.06	3.29	3.42	3.40	3.87

Tables S5. The zero-point energy (E_{ZPE}) and the product (TS) of temperature (T = 298.15 K) and entropy (S) of the relevant species, where asterisk (*) denotes the adsorption site.

Species	E_{ZPE} (eV)	TS (eV)
H_2O	0.56	0.67
H_2	0.27	0.41
O*	0.06	0.07
OH*	0.36	0.09
OOH*	0.45	0.18
*	0.00	0.00

Table S6. Theoretical characteristic vibration frequency of infrared absorption spectrum.

	Co-OOH	Co-OH	Co-O	Mn-OH
Wavenumber (cm^{-1})	3447.58	3614.18	620.64	3690.79
	1363.61	952.79	198.02	822.17
	868.86	525.99	133.32	538.27
	489.50	382.79		268.92
	386.35	183.87		109.53
	235.91	143.50		78.39
	173.16			
	103.32			
	91.46			

Calculation of turnover frequency (TOF) for electrochemical H_2O_2 production

To compare the activity of various catalysts (e.g. noble / non-noble metal and non-metal catalysts), we normalized the mass activity by the total weight of the catalyst and the weight of the active metal component only (see Fig. 2e). Activity of different catalysts was also evaluated by comparing their turn over frequency (TOF) values which consider the differences in the site density of various catalysts. TOF is the total number of molecules transformed into the desired product by one active site per time. In this study, the TOF values of catalysts were calculated for the $2e^-$ ORR pathway to evaluate the efficiency of electrochemical H_2O_2 production. The equation for deriving TOF is as follows.

TOF (s^{-1}) = (number of oxygen molecules turnover) / (number of active sites) = (j/2F) / n, j is the current density for H_2O_2 production measured from ring electrode with the collection efficiency of our RRDE setup at a given overpotential, F is the faraday constant (96,485 C mol^{-1}), and n is the number of active sites. (j/2F) stands for the total oxygen turnover in $2e^-$ ORR.

The number of oxygen molecules turnover was calculated as follows.

$$\text{(number of oxygen molecules turnover)} = \text{j}\left[\frac{\text{mA}}{cm^2}\right] \times \frac{1\,[C/s]}{1000\,[mA]} \times \frac{1\,[mol\,e^-]}{96485\,[C]} \times \frac{1\,[mol\,O_2]}{2\,[mol\,e^-]} \times \left(6.02 \times 10^{23}\left[\frac{atom\,O_2}{mol\,O_2}\right]\right)$$

The number of active sites was calculated as follows.

$$\text{(number of active sites)},\ n = L\left[\frac{mg}{cm^2}\right] \times R\,[\text{wt\%}] \times \frac{1\,[mmol]}{W\,[mg]} \times \left(6.02 \times 10^{20}\left[\frac{atom}{mmol}\right]\right)$$

L is the amount of catalyst loaded on the electrode, *R* is the weight fraction, and *W* is

the atomic weight of the corresponding element of active sites.

For the catalysts containing noble metals, all the noble metal centers were assumed as the active sites. Also, it has been demonstrated that the carbon atoms adjacent to several oxygen functional groups can be an active site for $2e^-$ ORR for non-metal carbon catalysts. Thus, we calculated the number of active sites on those carbon catalysts from the oxygen content of the surface.

References

1 G. Kresse, J. Furthmu¨ller, *Phys. Rev. B* 1996, **54**, 11169.

2 P. E. Blöchl, *Phys. Rev. B* 1994, **50**, 17953–17979.

3 J. P. Perdew, K. Burke, M. Ernzerhof, *Phys. Rev. Lett.* 1996, **77**, 3865–3868.

4 S. Grimme, J. Antony, S. Ehrlich, H. Krieg, *J. Chem. Phys.* 2010, **132**, 154104.

5 S. Dudarev, G. Botton, *Phys. Rev. B* 1998, **57**, 1505–1509.

6 H. Xu, D. Cheng, D. Cao, X. C. Zeng, *Nat. Catal.* 2018, **1**, 339–348.

7 H. J. Monkhorst, J. D. Pack, *Phys. Rev. B* 1976, **13**, 5188–5192.

8 J. K. Nørskov, J. Rossmeisl, A. Logadottir, L. Lindqvist, J. R. Kitchin, T. Bligaard, H. Jónsson, *J. Phys. Chem. B* 2004, **108**, 17886–17892.

9 http://webbook.nist.gov/chemistry/.

10 X. Guo, S. Lin, J. Gu, S. Zhang, Z. Chen, S. Huang, *ACS Catal.* 2019, **9**, 11042–11054.

11 C. Ling, L. Shi, Y. Ouyang, X. C. Zeng, J. Wang, *Nano Lett.* 2017, **17**, 5133–5139.

12 J. Gao, H. bin Yang, X. Huang, S. F. Hung, W. Cai, C. Jia, S. Miao, H. M. Chen, X. Yang, Y. Huang, T. Zhang, B. Liu, *Chem* 2020, **6**, 658–674.

13 S. Siahrostami, A. Verdaguer-Casadevall, M. Karamad, D. Deiana, P. Malacrida, B. Wickman, M. Escudero-Escribano, E. A. Paoli, R. Frydendal, T. W. Hansen, I. Chorkendorff, I. E. L. Stephens, J. Rossmeisl, *Nat. Mater.* 2013, **12**, 1137–1143.

14 A. Verdaguer-Casadevall, D. Deiana, M. Karamad, S. Siahrostami, P.

Malacrida, T. W. Hansen, J. Rossmeisl, I. Chorkendorff, I. E. L. Stephens, *Nano Lett.* 2014, **14**, 1603–1608.

15 J. S. Jirkovský, I. Panas, E. Ahlberg, M. Halasa, S. Romani, D. J. Schiffrin, *J. Am. Chem. Soc.* 2011, **133**, 19432–19441.

16 S. Yang, J. Kim, Y. J. Tak, A. Soon, H. Lee, *Angew. Chem. Int. Ed.* 2016, **55**, 2058–2062.

17 C. H. Choi, M. Kim, H. C. Kwon, S. J. Cho, S. Yun, H. T. Kim, K. J. J. Mayrhofer, H. Kim, M. Choi, *Nat. Commun.* 2016, **7**, 10922.

18 A. Wang, A. Bonakdarpour, D. P. Wilkinson, E. Gyenge, *Electrochim. Acta* 2012, **66**, 222–229.

19 D. Iglesias, A. Giuliani, M. Melchionna, S. Marchesan, A. Criado, L. Nasi, M. Bevilacqua, C. Tavagnacco, F. Vizza, M. Prato, P. Fornasiero, *Chem* 2018, **4**, 106–123.

20 Y. Sun, I. Sinev, W. Ju, A. Bergmann, S. Dresp, S. Kühl, C. Spöri, H. Schmies, H. Wang, D. Bernsmeier, B. Paul, R. Schmack, R. Kraehnert, B. Roldan Cuenya, P. Strasser, *ACS Catal.* 2018, **8**, 2844–2856.

21 E. Jung, H. Shin, B. H. Lee, V. Efremov, S. Lee, H. S. Lee, J. Kim, W. Hooch Antink, S. Park, K. S. Lee, S. P. Cho, J. S. Yoo, Y. E. Sung, T. Hyeon, *Nat. Mater.* 2020, **19**, 436–442.

22 R. Shen, W. Chen, Q. Peng, S. Lu, L. Zheng, X. Cao, Y. Wang, W. Zhu, J. Zhang, Z. Zhuang, C. Chen, D. Wang, Y. Li, *Chem* 2019, **5**, 2099–2110.

23 H. Li, P. Wen, D. S. Itanze, Z. D. Hood, S. Adhikari, C. Lu, X. Ma, C. Dun, L. Jiang, D. L. Carroll, Y. Qiu, S. M. Geyer, *Nat. Commun.* 2020, **11**, 3928.

24 K. Jiang, S. Back, A. J. Akey, C. Xia, Y. Hu, W. Liang, D. Schaak, E. Stavitski, J. K. Nørskov, S. Siahrostami, H. Wang, *Nat. Commun.* 2019, **10**, 3397.